

Excellence in Chemistry Research



Announcing our new flagship journal

- Gold Open Access
- Publishing charges waived
- Preprints welcome
- Edited by active scientists









Luisa De Cola Università degli Studi di Milano Statale, Italy



Ive Hermans
University of
Wisconsin-Madison, USA



Ken Tanaka Tokyo Institute of Technology, Japan

Check for updates



www.chemsuschem.org

Photoexcitation of Fe₃O Nodes in MOF Drives Water Oxidation at pH = 1 When Ru Catalyst Is Present

Roman Ezhov,^[a] Alireza K. Ravari,^[a] Mark Palenik,^[b] Alexander Loomis,^[a] Debora M. Meira,^[c] Sergei Savikhin,^[a] and Yulia Pushkar*^[a]

Artificial photosynthesis strives to convert the energy of sunlight into sustainable, eco-friendly solar fuels. However, systems with light-driven water oxidation reaction (WOR) at pH=1 are rare. Broadly used $[Ru(bpy)_3]^{2+}$ (bpy=2,2'-bipyridine) photosensitizer has a fixed +1.23 V potential which is insufficient to drive most water oxidation catalysts (WOCs) in acid, while Fe₂O₃, featuring the highly oxidizing holes, is not stable at low pH. Here, the key examples of Fe-based metal-organic framework (MOF) water oxidation photoelectrocatalysts active at pH=1 are presented. Fe-MIL-126 and Fe MOF-dcbpy structures were formed with 4,4'-biphenyl dicarboxylate (bpdc), 2,2'-bipyridine-5,5'-dicarboxylate (dcbpy) linkers and their mixtures. Presence of dcbpy linkers allows integration of metalbased catalysts via coordination to 2,2'-bipyridine fragments. Fe-based MOFs were doped with Ru-based precursors to achieve highly active MOFs bearing [Ru(bpy)(dcbpy)(H₂O)₂]²⁺

WOC. Materials were analyzed with X-ray diffraction (XRD), scanning electron microscopy (SEM), Fourier transform infra-red (FTIR) spectroscopy, resonance Raman, X-ray absorption spectroscopy, fs optical pump-probe, electron paramagnetic resonance (EPR), diffuse reflectance and electric conductivity measurements and were modeled by band structure calculations. It is shown that under reaction conditions, Fe^{III} and Ru^{III} oxidation states are present, indicating rate-limiting electron transfer in MOF. Fe₃O nodes emerge as photosensitizers able to drive prolonged O₂ evolution in acid. Further developments are possible via MOF's linker modification for enhanced light absorption, electrical conductivity, reduced MOF solubility in acid, Ru-WOC modification for faster WOC catalysis, or Ru-WOC substitution to 3d metal-based systems. The findings give further insight for development of light-driven water splitting systems based on Earth-abundant metals.

Introduction

Matching the rapid increase of global demand for energy largely depends on traditional fossil fuel consumption, especially in emerging market economies. This creates new economical, societal, and ecological challenges, since higher consumption of fossil fuels leads to higher greenhouse gas emissions, particularly carbon dioxide (CO₂). The threats of global warming and climate change motivate development of new technologies to reduce CO₂ emissions. Hydrogen gas seems to be the best energy carrier since it forms just water and has the highest energy value upon combustion on air among other chemical fuels (141.8 MJ/kg). Our goal is to develop economically viable

industrial-scale hydrogen production using practically unlimited resources – water and sunlight – without destructive emissions (artificial photosynthesis). Since noble-metal based coordination compounds are effective in water splitting catalysis, our goal is to optimize their usage and potentially substitute them in the future for efficient 3d metal-based WOCs making these catalysts economically feasible. The main challenge in electrochemical water splitting for hydrogen production is the multi-electron water oxidation reaction (WOR), $2H_2O \rightarrow O_2 + 4e^- + 4H^+$, enabling the hydrogen gas formation via the proton reduction: $4H^+ + 4e^- \rightarrow 2H_2$. Thus, conversion of sunlight into chemical energy requires a photocatalytic material able to work in acidic media with high WOR effectiveness and durability in the highly oxidizing chemical environment required for WOR.

WOC systems operational at acidic pH are crucial for high purity hydrogen production and have distinctive technological advantages, such as compatibility with existing fuel cell technologies and –proton-exchange membrane (PEM) for integration with electrolyzing devices operating at high current densities and pressure. [2] In basic and neutral conditions, the issues associated with water splitting comprise limited PEM ionic conductivity, slow kinetics, and sensitivity toward impurities. [3] On the other hand, water splitting and hydrogen formation in acidic conditions are beneficial due to the high proton concentration, enabling PEM to operate at high current densities (>1 A/cm²), minimizing crossover and resistance losses. [4] Low stability and performance of WOCs at low pH are attributed to intense degradation of the catalytic material in acidic media, highly oxidative environment of WOR and energy

[b] Dr. M. Palenik US Naval Research Laboratory Washington, 20375 (USA)

[c] Dr. D. M. Meira Argonne National Laboratory Argonne, IL 60439 (USA)

Supporting information for this article is available on the WWW under https://doi.org/10.1002/cssc.202202124

© 2022 The Authors. ChemSusChem published by Wiley-VCH GmbH. This is an open access article under the terms of the Creative Commons Attribution Non-Commercial License, which permits use, distribution and reproduction in any medium, provided the original work is properly cited and is not used for commercial purposes.

 [[]a] Dr. R. Ezhov, Dr. A. K. Ravari, A. Loomis, Dr. S. Savikhin, Dr. Y. Pushkar Department of Physics and Astronomy Purdue University West Lafayette, 47907 (USA) E-mail: ypushkar@purdue.edu



losses due to high overpotential.^[5] Nevertheless, WOCs based on iridium and ruthenium oxides are currently considered to be the most active and stable catalysts in oxygen evolution reaction (OER) at acidic pH.^[6] However, the high cost of these materials motivates the development of more effective catalysts with lower content of the precious metals and lesser intrinsic limitations.

Multiple light-responsive systems based on metal oxides have been evaluated as photoanodes in various photocatalytic applications.[7] One of the most studied systems for photocatalytic water splitting is the TiO2-based family of the photoanodes.^[7a,8] However, these catalysts limit their photocatalytic efficiency to the UV region of sunlight due to the large bandgap (3.2 eV). Overall, only about 5% of the solar spectrum can be utilized in water-splitting transformations using TiO₂based photocatalytic systems.^[9] Solar light contains about 50% of the photons with $400 < \lambda < 800$ nm, making development of photocatalysts capable of activation under visible light essential. Outfitting the TiO₂ with different inorganic moieties is a popular strategy towards constructing composite materials photo-responsive to visible light. [8b,10] Nevertheless, the modifications of TiO₂ photoelectrodes are limited to basic water solutions, doping with metal centers, and combination with other semiconductors. BiVO₄ and WO₃ were also broadly used in photocatalytic assemblies due to extension of their absorption up to 520 nm into the visible light and satisfactory stability in acidified solutions.[11] But modification of these photocatalysts toward better performance is difficult due to their fixed chemical structure, bandgaps in the approximately 2.4-2.5 eV range and reliance on material morphology engineering for improved performance. Thus, more universal and adaptable photocatalytic assemblies should be developed.

Iron oxide, Fe_2O_3 , has considerable photocatalytic potential due to a lower bandgap value (around 2.2 eV) and absorbance of visible light up to about 600 nm. [7c,8b,12] However, the high recombination rate of photoinduced charge-separated states significantly limits its practical application. There are a few approaches to overcome high recombination rates, such as outfitting a photocatalytic material with another active center to improve an overall catalytic performance of the obtained composite. [7c,13]

Metal-organic frameworks (MOFs) are particularly convenient type of heterogeneous photocatalytic assemblies for WOR due to tunability of physical properties: high surface area, porosity that enables chemical and charge transfer, and crystalline nature. Applications of MOFs in photocatalysis to promote hydrogen evolution and WOR are currently emerging.[14] MOF functionalization drastically affects its photocatalytic performance and allows ligand modification, metal doping or topological variability due to the different synthetic conditions (presence of a modulator, temperature etc.).[15] A few factors favor photocatalytic activity of MOFs. [14b,16] Effective light capture and charge separation play crucial roles, along with MOF conductivity and reactivity of a catalytic center. Organic ligand modification is particularly popular, since it shifts the light absorption range along with a bandgap energy and opens a way for additional structural development. Doping of MOFs bearing a chelate group, like bipyridine, as well as anchoring of MOF's functional group with catalytic metal moieties are widely studied and allows preparation of frameworks that can be used in a great variety of applications. Until recently, the Zrbased UIO family of MOFs was studied in its photocatalytic performance under UV-light. Nevertheless, wide band gap (about 3.7 eV) of Zr-based MOFs leading to the lack of photoactivity in visible range, limited conductivity, and stability for long-term storage and usage encouraged us to study other MOFs with similar molecular architecture.

Among the metals used in MOF metal nodes, iron has unmatched advantages as a cheap Earth-abundant and environmentally benign element. Iron-based MOFs are remarkably diverse, easy to prepare, and relatively stable for long-term storage. [21] Some Fe-based MOFs with [Fe₃O(X)_n] motive (where X is a carboxylate, Cl⁻ or water ligand to Fe) appear to be active in Fe₃O-driven photocatalytic CO₂ reduction^[22] and water splitting at neutral and basic pH with an action spectrum throughout a visible range.[17c,23] In this study, we present Fe MOF based photoelectrochemical anodes with general formula $[Fe_3O(O_2C-R-CO_2)_6(H_2O)_2CI]$ $(R = biphenyl or bipyridyl)^{[21a,24]}$ doped with Ru complex capable of oxidizing water at pH=1. These MOFs consist of Fe µ-oxo nodes as primary photoresponsive units interconnected with diaryl organic linkers. Fe MOFs isostructural to Fe MIL-126 were achieved with 4,4'biphenyl dicarboxylate (bpdc) linker as well as mixture of bpdc and 2,2'-bipyridine-5,5'-dicarboxylate (dcbpy) linkers (up to 75%). These Fe-MOFs were doped with Ru-based molecular WOC using different synthetic approaches and their photoelectrocatalytic activity in acidic media was demonstrated. Rudoped Fe MOF with dcbpy linkers (Fe MOF-dcbpy, 100% of dcbpy), is similarly photoelectrocatalytically active even though it has a different three-dimensional (3D) structure. Despite the reported sensitivity of the iron-based nodes to the acidic conditions,[25] we were able to stabilize these materials on fluorine-doped tin oxide (FTO) glass electrode for prolonged photoelectrocatalytic water oxidation at pH=1 using a protonconductive polymeric membrane. The materials were also analyzed with X-ray diffraction (XRD), scanning electron microscopy (SEM), Fourier transform infra-red (FTIR) spectroscopy, resonance Raman, X-ray absorption spectroscopy, fs optical pump probe, electron paramagnetic resonance (EPR) and electric conductivity measurements. Density functional theory (DFT) calculations of the band structure of the Fe-MOF assisted in understanding the nature of its interaction with light. Prolonged photoelectrochemical O₂ evolution activity was demonstrated for Fe-MOFs with bpdc and dcbpy linkers doped with [Ru(bpy)(dcbpy)(H₂O)₂]²⁺ molecular WOC.

Results and Discussion

Synthesis and characterization

MOF preparation and structure determination

The MOFs with Fe μ -oxo nodes interconnected with bpdc, the mixtures of bpdc and dcbpy (up to 75%) and 100% dcbpy linkers were prepared using solvothermal synthesis similar to Fe MIL-126 MOF preparation procedure reported earlier (Supporting Information, Section S1).[24a] Powder XRD (PXRD) data for all prepared materials are shown (Supporting Information, Section S2, Figure S1). Fe MIL-126, MOF-1, MOF-2 and MOF-3 crystalline structures are in agreement with the simulated PXRD patterns of Fe MIL-126 MOF based on CCDC deposited structure (Figure S1A and B). [15c,24a] It was found that MIL-126 topology of the MOFs with mixed bpdc and dcbpy linkers persists for 50% and 75% dcbpy content if trace amounts of pure Fe MIL-126 phase present in the reaction vessel (otherwise an amorphous material may be formed). The MOFs with 100% dcbpy linker content (Fe MOF-dcbpy) and its derivative MOF-4 have the crystalline structure reported earlier, although their molecular architecture is not known with certainty (Figure S1C) (see also Figure S38 in Bara et al., **JACS** 2019, Supporting Information). [24a,26] Preparation of Fe MOF-dcbpy with acetic acid (AcOH) as a modulator leads to similar crystalline product to the one reported earlier using trifluoracetic acid (TFA) modulator. From chemical viewpoint there is little difference between AcOH and TFA except lower acidity of AcOH. Structural resemblance of TFA and AcOH suggests similar modulation mechanism when the acid temporarily ligates Fe₃O oxo nodes, thus slowing MOF crystal growth. Our attempt to reproduce the procedure from Bara et al. 2019[24a] with TFA as a modulator resulted in the formation of the same product as with AcOH (Figure S1C).

The catalytic materials were prepared by doping the MOFs with Ru catalyst (Figure 1) using three methods: 1) postsynthetic bpdc linker exchange of Fe MIL-126 with dcbpy moiety of Ru-catalyst (MOF-1), similarly to the earlier reported functionalization of the Zr-based UIO-67 $\mathrm{MOF}^{:[27]}_{r}$ 2) synthesis of Ru-doped Fe MIL-126 MOF in the presence of presynthesized [Ru(bpy)(dcbpy)(H₂O)₂]²⁺ catalyst (MOF-2); 3) on-MOF doping of dcbpy-linker in the mixed-linker bpdc:dcbpy 1:1 Fe MIL-126 (MOF-3) and in 100% dcbpy MOF (MOF-4) with Ru-(bpy)(cymene)Cl₂ precursor. [14c,15c,17a,27,28] Crystalline structure of all the MOFs after doping with Ru-catalyst remains intact at given Ru-catalyst content (Figure S1). We used 1:12 ratio of Ru precursors Ru(bpy)(cymene)Cl₂, [Ru(bpy)(dcbpy)(H₂O)₂]²⁺ and Ru(bpy)(dcbpy)Cl₂ to the linkers of all the MOFs due to earlier findings for the optimal ratio of Ru WOC to the linker in UIO-67 MOF for preservation of the sample crystallinity. [27,29] For the control experiments UIO-67 MOF with dcbpy linkers was prepared using known procedures with subsequent on-MOF doping by the catalyst precursor Ru(bpy)(cymene)Cl₂ (Figure S1E).[30] Higher molar ratio of Ru WOC precursor to linker leads to the PXRD-visible degradation of crystalline structure of

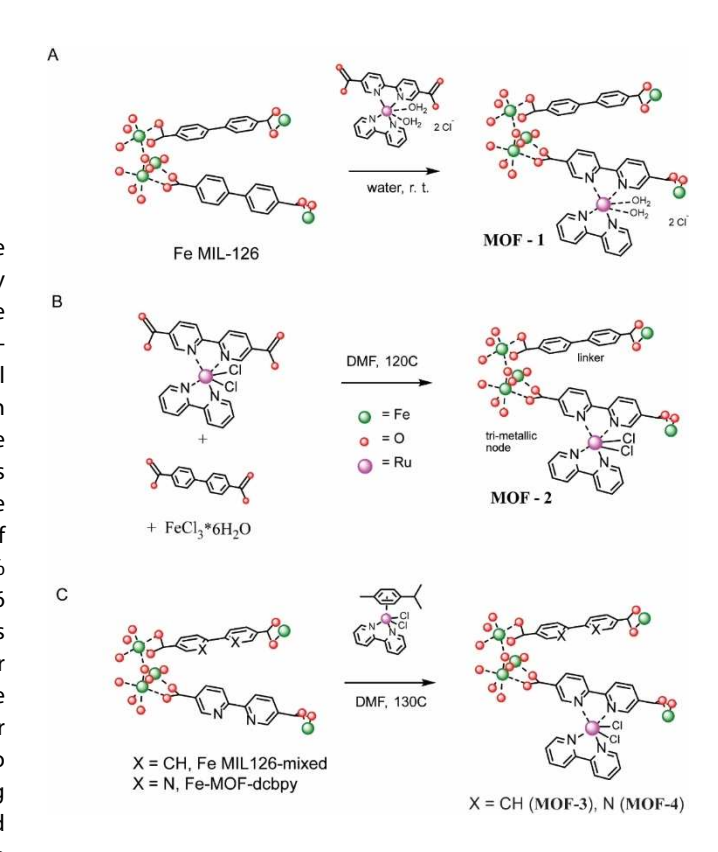


Figure 1. Synthetic scheme for doping of Fe-MIL MOFs with Ru-catalyst: (A) postsynthetic linker exchange, (B) MOF synthesis in the presence of Ru-WOC, (C) on-MOF linker doping.

the MOFs due to disruption of the crystalline framework by multiple Ru(bpy)(dcbpy) moieties.

SEM imaging shows that MOFs 1, 2 and 3 with Fe MIL-126 topology form octahedral crystals (Supporting Information, Section S2, Figure S2) whereas MOF-4 with the different linker network (dcbpy) has similar morphology to the Fe MIL-88 samples featuring the hexagonal rods (Figure S3). [24a] The crystalline profile of MOF-4 persists even for material used as photoanode over two days in an electrochemical cell (see below), although sharp crystal edges become less prominent (Figure S4).

The electric conductivity of Fe MIL-126 was measured to be 3.3×10^{-9} S/cm using custom-made conductivity measurement device (Figure S5). Conductivity of Fe MOF-dcbpy and MOF-4 were on par with the sensitivity of our measurement and was estimated to be around or below 1×10^{-11} S/m. Obtained results are comparable to other Fe-based MOFs reported previously.^[31]

FTIR spectra of as-prepared MOFs show the presence of carbonyl group vibrations in 1290–1672 cm⁻¹ range (Figure S6) and other bands characteristic of 4,4′-dicarboxybiphenyl and 5,5′-dicarboxy-2,2′-bipyridyl moieties.^[32] The prominent peaks around 1600 cm⁻¹ and 1390 cm⁻¹ indicate asymmetric and symmetric stretching vibrations of the carbonyl groups with likely bidentate coordination.^[26] Similarity of FTIR spectra of the MOFs before and after doping with Ru in combination with unchanged PXRD pattern also confirms that MOF crystalline structure remains unchanged with the Ru doping.

Α

3, 5, Downloaded from https://chemistry-europe.onlinelibrary.wiley.com/doi/10.1002/cssc.202202124 by Purdue University (West Lafayette), Wiley Online Library on [08.06/2023], See the Terms and Conditions (https://onlinelibrary.wiley.com/terms-and-conditions) on Wiley Online Library for rules of use; OA articles are governed by the applicable Creative Commons

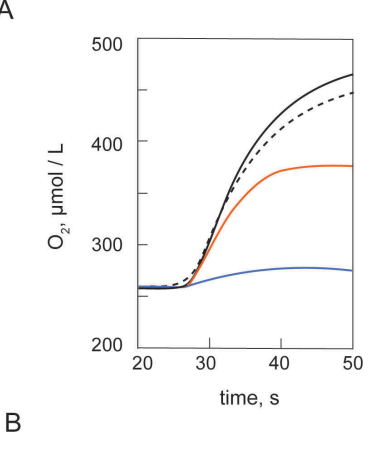
UV-visible diffuse reflectance spectra show the absorbance bands extended to visible light region for all the MOFs except undoped UIO-67-dcbpy prepared as a control material (Figure S7). Intensity of the absorbance correlate with Ru doping.^[28,33] However, we have not observed an immediate connection between the absorbance and photoelectrochemical WOR performance which indicates that not all "colored" components of the system are photoactive for water oxidation. For instance, Ru WOCs with the polypyridine ligands are brightly colored but not photoactive. MOF-4 and parent Fe MOF-dcbpy have darker color appearance in comparison to Fe MIL-126 likely due to some minor chelating of Fe ion by 2,2'bipyridine fragments, as mentioned in earlier literature. [24a] Diffuse reflectance spectra plots for the Ru-undoped MOFs built after Kubelka-Munk transformation (Figure S8) confirm presence of 1.75-2.4 eV bandgap for the Fe-based MOFs (Fe MIL-126 and Fe MOF-dcbpy) and 3.45 eV for Zr-based UIO-67. This bandgap for Fe-based MOFs is in agreement with DFT calculations (see below).

EPR spectra of Fe MOF-dcbpy and MOF-4 suspension in 0.1 M HNO₃ taken at 20 K agree with Fe³⁺ oxidation state, while a weak Ru³⁺ signal can be detected for MOF-4 (Figure S9). The Ru³⁺ state in MOF-4 is a result of its oxidation by diluted nitric acid.

Activity of the MOFs in chemically driven water oxidation catalysis

The MOFs prepared by different methods (MOF-1, MOF-2, MOF-3 and MOF-4) were tested in WOR promoted by excess of cerium (IV) ammonium nitrate (CAN) at pH=1 using a Clarktype oxygen electrode of the Oxygraph (see Experimental Section, S6). Before, the experiment ruthenium-doped MOFs were mixed with 0.1 M HNO₃ for 30 minutes to promote hydrolysis of the Ru-Cl moiety into Ru-(H2O), necessary for water oxidation catalysis. [34] For Ru(bpy)₂Cl₂ complex in solution exchange of Ru-Cl coordination to Ru-H₂O is almost instantaneous and Ru(bpy)(dcbpy)Cl₂ post-synthetically incorporated into UIO-67 also demonstrated complete Ru-CI exchange per extended X-ray absorption fine structure (EXAFS) analysis. [27] Note that post-synthetic exchange mostly decorates Ru complexes close to the MOF surface. However, EXAFS monitoring of Ru–Cl interaction in [Ru(tpy)(bpy)Cl]-UIO-67 (tpy = 2,2':6',2''terpyridine) demonstrated that Ru-Cl does not fully exchange even after 24 h. [16c] EXAFS analysis of MOF-1 and MOF-4 mixed with CAN and quickly frozen shows that some Ru-Cl interactions were retained (Figure S12, Table S1A,B, see below) similarly to the [Ru(tpy)(bpy)Cl]-UIO-67 system. [16c] While quantitative analysis of N-numbers per EXAFS carries large error we can estimate that around 25% of Ru-Cl bonds are retained under the condition of quick mixing CAN experiment.

Oxygen evolution rate was measured as a function of time (Figure 2A). These experiments revealed that MOF-1, prepared by linker postsynthetic exchange with 1:12 Ru-catalyst to bpdc linker ratio has the highest CAN-induced activity in WOR with initial oxygen evolution rate of about 14 nmol/s·ml while MOF-



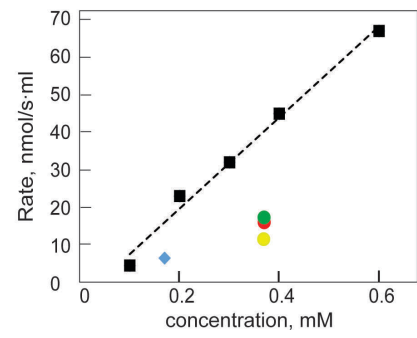


Figure 2. (A) Representative oxygen evolution catalyzed by MOF-1 (black), MOF-2 (blue), MOF-3 (orange), MOF-4 (dashed) in chemically driven WOR with CAN at pH = 1. (B) Comparison of oxygen evolution activity of MOFs with molecular catalyst [Ru(bpy)(dcbpy)(H₂O)₂]²⁺ and Ru-doped UIO-67 MOF in CAN promoted WOR at pH = 1: black squares- $[Ru(bpy)(dcbpy)(H_2O)_2]^{2-}$ blue rhomb-UIO-67 doped with [Ru(bpy)(dcbpy)(H₂O)₂]²⁺ by post-synthetic linker exchange method, [27] green round–MOF-1, yellow round–MOF-3, red round-MOF-4. Dashed line in Figure 2B indicates first order dependance of O_2 evolution on the molecular catalyst $[Ru(bpy)(dcbpy)(H_2O)_2]^{2+\frac{1}{2}}$

2 with Ru-WOC in volume features an oxygen evolution rate of 2.6 nmol/s·ml. MOF-4, prepared by linker doping with the catalyst precursor, shows rather high oxygen evolution rate of around 12 nmol/s·ml comparable with approximately 10 nmol/ s·ml for MOF-3 (Figure 2). Thus, higher WOR activity of MOF-1 reflects sufficient surface localization of the Ru-catalyst while catalytic behavior of MOF-3 and MOF-4 might be ascribed to the surface localization as well as to 3D structure where more Ru centers are accessible to the large Ce^{IV} ion.^[14c] Lower activity of MOF-2 in chemical WOR originates from distribution of the Ru catalytic centers inaccessible to Ce^{IV} inside bulk volume of the MOF. Non-doped Fe-MOFs (Fe MIL-126 and Fe MOF-dcbpy) were also tested in CAN oxidation at pH=1 in control experiments and demonstrated no oxygen evolution, thus confirming the -MOF-embedded Ru complex as a source of the catalytic activity.

To assess Ru catalytic centers retention in the MOFs in chemical WOR with CAN, Ru loading level was measured before and after water oxidation for MOF-4 as a representative example with average photoresponse (see below, Figure 5). Content of Ru(bpy)(dcbpy)Cl₂ precatalyst in as-prepared MOF-4 is 0.17 μ mol/1 mg of the MOF that corresponds to about 1:10



molar ratio of the precatalyst to dcbpy linker of MOF-4. To determine whether the Ru catalyst is located on MOF surface or inside the pores, a Fe/Ru ratio has been calculated based on results of inductively coupled plasma mass spectrometry (ICP-MS) measurements. Initial MOF-4 material was found to have the element ratio Fe/Ru = 8.3. This implies the Ru catalyst is not located just on the MOF surface but also inside MOF-4 crystalline structure. Taking into account Fe-based MOF pore dimensions 10.2 Å and 27.6 Å^[21a] and about 10 Å size for [Ru(bpy)] moiety,[35] localization of the latter inside the MOF pores is possible during the conditions of on-MOF synthesis (Figure 1C). Following oxidation of MOF-4 in the Oxygraph chamber initial Fe/Ru = 8.3 ratio changes to Fe/Ru = 7.7, indicating that a significant amount of Ru complex is still retained in the pores. However, recovered MOF-4 showed only negligible CAN-promoted water oxidation activity, although the MOF crystalline structure undergoes only minor changes (Figure S1D). This implies that surface catalytic centers might have been lost or otherwise deactivated.

A minimal turnover number (TON) for MOF-4 was calculated from the oxygraph data for the first 5 minutes of the WOR (Figure S10). At pH=1 a value TON=105 was obtained after 5 minutes of water oxidation with large excess of CAN. Longer measurements lead to the damage of an oxygraph membrane in harsh oxidative conditions and subsequent data error.

Assessment of O_2 evolution rates for Fe-based MOFs and the previously reported rate for Ru-doped UIO-67 MOF^[27] in water oxidation with CAN at pH=1 shows comparable activity relative to the solution of free catalyst [Ru(bpy)(dcbpy)(H₂O)₂]²⁺ (Figure 2B, red, green and yellow dots).

Rapid (tens of seconds) reduction of oxygen evolution in CAN – driven WOR of the MOFs (Figure 2A) is attributed to quick desorption of catalytically active centers from the MOF surface due to the harsh water oxidation environment (combination of low pH and strong oxidizer).

Spectroscopic characterization of the MOF materials in chemically driven WOC

X-ray absorption spectroscopy (XAS, and EXAFS) and resonance Raman (RR) spectroscopy techniques were used to follow the material transformations and possible reactive species of the MOFs during CAN-promoted water oxidation catalysis (Figure 3, and Supporting Information Section S8, S9).

X-ray absorption near edge structure (XANES) and EXAFS were performed for the MOFs bearing different linker environment (bpdc and dcbpy) and oxidized with CAN followed by quick (tens of seconds) freeze quench in liquid N_2 (Figure 3, S11-S13). Ru K-edge XANES of oxidized MOFs confirmed the transition of Ru^{\parallel} state in the initial MOFs to the Ru^{\parallel} upon addition of CAN at pH=1. Previous observations of redox behavior of molecular $[Ru(bpy)(dcbpy)(H_2O)_2]^{2+}$ catalyst in acidic solution revealed the formation of Ru^V species upon oxidation with CAN at pH=1 and fast freezing in liquid N_2 . [27] In spite of prominent water oxidation activity, oxidized MOF-1 and MOF-4 samples prepared in the same conditions did not exhibit

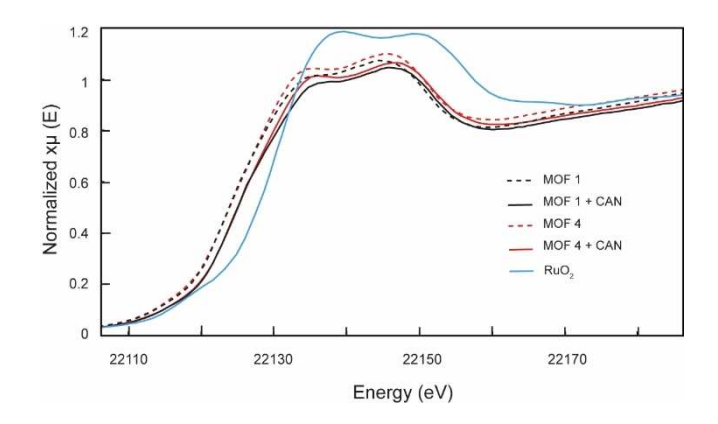


Figure 3. Ru K-edge XANES of the MOFs with different linker framework (bpdc and dcbpy) before (dashed curves) and after oxidation with CAN at pH=1 (solid curves) in comparison with RuO₂ (blue curve).

highly oxidized Ru intermediates (Ru^{IV} or Ru^V states) in XANES, similar to the case of oxidation of the Ru based WOCs incorporated into UIO-67. This may be a result of low population of highly oxidized Ru species in MOF due to their short lifetime and rate-limiting electron transfer to Ce^{IV} ions through the MOF material. XANES of recovered MOF-4 obtained after oxidation with CAN also confirmed the Ru^{III} oxidation state (Figure S11), showing that system does not return to Ru^{II}.

Fourier-transformed EXAFS of the MOF-1 and MOF-4 immediately frozen in liquid N_2 after CAN addition confirmed Ru^{III} environment as of the molecular complex [Ru^{III}(bpy)(dcbpy)] (Figure S12, Table S1). For MOF-1 and MOF-4 oxidized with CAN at pH = 1, two prominent EXAFS peaks correspond to the first (Ru–N and Ru–O, about 2.0 Å) and second (Ru–C, around 3.0 Å) coordination spheres with smaller Ru–Cl peak (around 2.3 Å) seen in between (Figure S12C). Retention of some Ru–Cl bonds highlights the difficulty of Cl exchange throughout the MOF structure.

Fe K-edge XANES data of the MOFs were similar to the previously reported Fe XANES of Fe-MIL-100^[36] and indicated all Fe^{III} state (Figure S13). No changes in iron oxidation state have been detected when Fe MOFs were treated with CAN, except the case of MOF-4 featuring a shift of Fe K-edge toward the Fe^{IV} state. We speculate that catalyst insertion led to the partial opening of the MOF-4 structure, making Fe centers in the nodes accessible to CAN oxidation. Alternatively, these "oxidizable" Fe centers might be Fe ions coordinated to nitrogen of dcbpy linker, as was described previously.^[37]

Resonance Raman spectra were recorded for the MOFs at two wavelengths: 532 nm (Figure S14) and 638 nm (data not shown), with little difference in spectra showing that Fe-MOF absorption extends beyond 600 nm (this agrees with the diffuse reflectance data, Figure S7). The bands visible around 620 cm $^{-1}$ are similar to the Fe $_3$ O μ -oxo cluster vibrations. $^{[26]}$ The major bands around 1600 cm $^{-1}$ are aromatic vibrations in the linkers. The bands in the range of 1200 cm $^{-1}$ to below 1600 cm $^{-1}$ can be assigned to the carboxylate group (C–O, C=O, O–H). Fe MOF-dcbpy and MOF-4 RR spectra recorded at 532 nm are identical due to the lack of selective resonance effect for MOF

Chemistry Europe European Chemical Societies Publishing 5, 5, Downloaded from https://chemistry-europe.onlinelibrary.wiley.com/doi/10.1002/cssc.202202124 by Purdue University (West Lafayette), Wiley Online Library on [08/06/2023], See the Terms and Conditions (https://onlinelibrary.wiley.com/terms-and-conditions) on Wiley Online Library for rules of use; OA articles are governed by the applicable Creative Commons

with and without Ru complex (Figure S14A). CAN oxidation results in small changes in vibrations for these dcbpy-based MOFs. The major peak at 1050 cm⁻¹ is N-O vibration in a nitrate. The Ru^{IV}=O band at 800 cm⁻¹ was not observed here. This agrees with other spectroscopic characterization showing that MOF-4 contains Ru^{III} when oxidized with CAN (see XAS results). No ¹⁶O/¹⁸O isotope sensitive bands were detected for initial and CAN oxidized MOF-4 sample. Previously, we were able to use RR spectroscopy to observe oxidation of Ru complex to Ru^{IV}=O or Ru^V=O intermediates in Zr based MOF (UIO-67),[17a,27] but the same observation was not possible here due lack of these species and strong absorption/resonance enhancement by Fe MOF-dcbpy framework itself.

Electrochemical study of the electrodes with the photocatalytic layers

Deposition of the electrocatalyst on FTO glass electrodes surface was performed using two different methods: 1) thin film growth (GR) using solvothermal synthesis followed by Rucatalyst doping using on-MOF synthesis or post-synthetic ligand exchange with Ru-catalyst (GR-electrodes) and 2) drop-casting (DC) of the powder MOF on the electrode surface (DC-electrodes).

Cyclic voltammetry performed for the GR and DC electrodes at pH=1 features three consecutive oxidation processes Ru^{II}→ Ru^{III}, Ru^{III}→Ru^{IV}, and Ru^{IV}→Ru^V, accompanied by electrocatalytic current (Figure 4A, Table S2). This agrees with previous observations for cyclic voltammetry (CV) of [Ru(bpy)(dcbpy)(H₂O)₂]²⁺ WOC solution itself or embedded into the UIO-67 MOF grown on an FTO electrode. [27] Figure 4A shows the Ru^{II} \rightarrow Ru^{III} transition at around +0.7 V and the Ru^{III} \rightarrow Ru^{IV} transition at about +0.96 V vs. Ag/AgCl reference electrode (pH=1). At higher potential, Ru^{IV}→Ru^V oxidation occurs with onset of catalytic current at about + 1.4 V vs. Ag/AgCl reference electrode at pH = 1. Meanwhile, MOF-1(GR) electrodes demonstrated lower current likely due to the limited conductivity between the Ru complex localized on the surface after doping and FTO electrode. We did not observe any additional electrochemical features for the Fe MOF-dcbpy electrodes (Figure 4A) which indicates that Fe centers are likely all Fe^{III} at the range of applied potentials.

CV of MOF-4 photoanode was recorded during photoactivation with consecutive 1 min light/dark cycles continued for 20 minutes with around 500 W light source passed through UV-filter (CuSO₄ solution) (Figure S15). Ten overlayed CVs of the photoanode under light revealed depletion of the Ru^{II} to Ru^{III} redox transition accompanied by growth of a catalytic current (Figure S15B). This confirms light-driven oxidation of Ru centers in the material and accumulation of Ru^{III} as a resting state (Figure S15A).

Amperometric i-t curves of the MOF-based electrodes as the working anodes were collected in an electrochemical cell (chemical beaker) using a three-electrode configuration with Pt wire as a counter electrode, and an Aq/AqCl reference electrode at 1.4 V vs. Ag/AgCl at pH = 1. First, i-t curves of GR-electrodes were recorded without light illumination ("dark") (Figure 4B).

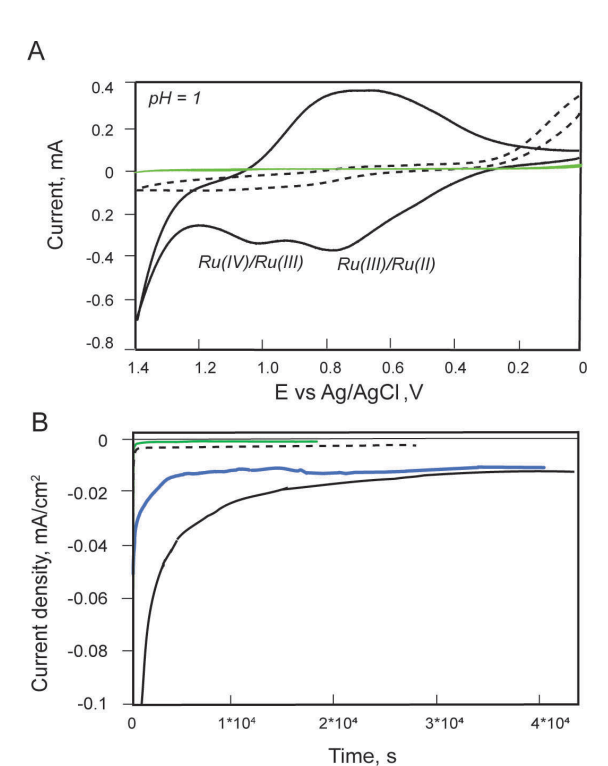


Figure 4. Electrochemical behavior of GR-electrodes with different linkers in the absence of light. (A) CV of MOF-4(GR) electrode (black solid curve) in comparison with CVs of MOF-1(GR) electrode (dashed curve) and Fe MOFdcbpy electrode (green curve) at pH = 1. (B) Amperometric i-t curves at 1.4 V vs. Ag/AgCl at pH = 1 for the MOF-4(GR) electrode (solid black curve), MOF-1(GR) electrode (dashed black curve), UIO-67 MOF doped with the same catalyst (blue curve) using post-synthetic modification procedure, [27] Fe MOFdcbpyelectrode (green curve).

Catalytic current of the MOF-4(GR)-electrode remains relatively stable for prolonged time, comparable with UIO-67 MOF doped with the same WOC (Figure 4B).[27] This encouraged us to develop more scalable system, namely, to drop-cast MOFs onto FTO glass electrodes. These DC-electrodes were prepared according to the reported procedure. [17c] Electrochemical redox behavior of DC-electrodes is similar to the GR-electrodes at the same pH with two redox transitions for Ru^{II}/Ru^{III} and Ru^{III}/Ru^{IV}.

A photoelectrochemical water-splitting device prototype with drop casted MOF photoanode firmly covered by a protonconductive Nafion membrane was assembled and tested in the electrochemical cell (Figure 5, S16, S17). It is obvious that structural stability of the photoanode in solution is crucial for its electrocatalytic activity during prolonged electrolysis. The Nafion layer can mitigate solubility effects and diffusion of the catalytic material away from the photoanode at applied potential. The MOF DC-photoanodes were tested for prolonged (>8 h) electrolysis at pH=1, 0.1 M HNO₃ at 1.4 V vs. Ag/AgCl applied potential (Figure 5). Only the bottom of the photoanode was submerged into the electrolyte. Photoanode testing was done in two segments: 1) activation: via saturation of Nafion film and drop-casted electrocatalytic layer with the electrolyte solution; 2) photo-assisted electrolysis with 1 minute light on/off for 21 minutes, after 10 minutes and 5 h from the

, 5, Downloaded from https://chemistry-europe-onlinelibrary.wiley.com/doi/10.1002/cssc.202202124 by Purdue University (West Lafsyette), Wiley Online Library on [08.06/2023]. See the Terms and Conditions (https://onlinelibrary.wiley.com/terms-and-conditions) on Wiley Online Library for rules of use; OA articles are governed by the applicable Centwise Commons of the Commons of the Conditions of the Commons of the Conditions of the Conditions

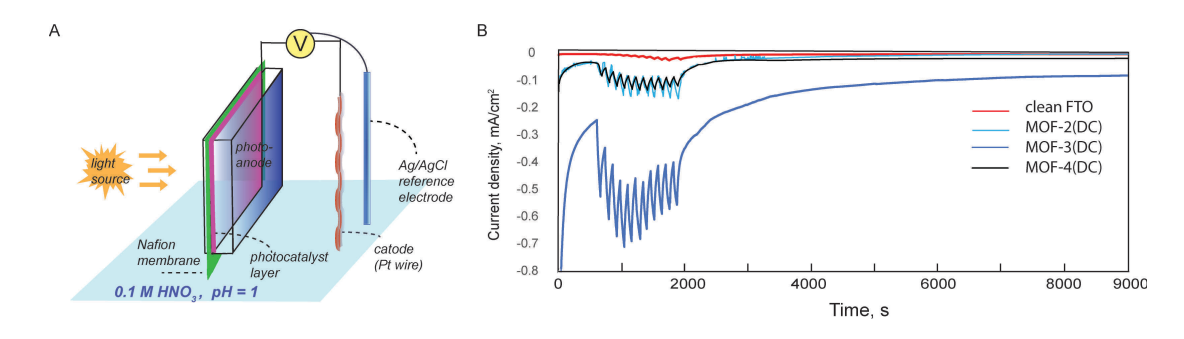


Figure 5. (A) Three-electrode electrochemical cell with the FTO working electrode with the drop-casted photoelectrocatalytic MOF layer confined by Nafion membrane, Pt-wire as the counter electrode, and Ag/AgCl as the reference electrode. (B) Comparison of photoelectrocatalytic performance for MOF-2 (DC), MOF-3(DC), MOF-4(DC) photoanodes at pH = 1. 11 light/dark cycles (1 minute light/1 minute dark) were applied 10 minutes from beginning of +1.4 V vs. AgCI/CI potential application to the activated electrode assembly (jagged path of the curves).

starting of potential application (Figure 5B, S16, S17). Long term stability (>8 h) of the photoelectrocatalytic layer without significant loss of the photo-response during prolonged electrolysis is shown in Figure S16. Under illumination, the photocatalytic current increases by more than one order of magnitude for MOF-2, -3, -4 photoanodes in acidic conditions (pH=1). Blank FTO glass electrode and Fe MOFs without Ru catalyst were used in the control experiments. MOF-1 photoanodes demonstrated much lower activity (Figure S16) in comparison with MOF-2 and MOF-4 photoanodes. This correlates with lesser Ru content in MOF-1 crystalline volume and localization of Ru catalyst on MOF surface after post-synthetic linker exchange. Photoresponse of the Ru-doped MOF during bulk electrolysis at pH=7 is similar to the one at pH=1(Figure S18). This may be due to pH-independent limiting charge transfer kinetics in non-conductive MOF material.

To confirm that the electrical current observed is the result of electrophotocatalysis, the MOF-4(DC) photoanode was tested in the generator-collector (GC) electrochemical cell (Figure 6A) at pH=1.[38] The GC cell was assembled according to the previously reported scheme with 1 mm space between the water oxidation MOF-4 photoanode and the oxygen reduction cathode - a blank FTO-glass. During the experiment, the generator electrode was at +1.4 V vs. Ag/AgCl potential while the collector electrode was at reducing potential of -0.45 V vs. Ag/AgCl in 0.1 M HNO₃. While the potentials were fixed for the duration of the experiment (30 minutes), a light was turned on and off every 2 minutes. Figure 6B shows the currents on the generator and collector. Blue and red stripes in this figure represent the time that light was turned off and on, respectively. Light illumination results in the increase in the current for both collector and generator electrodes. This is important that both currents change, since the increase of the current on the collector electrode assures that the increase in current for the generator is due to oxygen evolution rather than any other process.

The electrolysis with GC cell shows simultaneous change in electrocatalytic current in oxygen generation and oxygen reduction thus confirming the light-driven WOR of MOF-4(DC) catalytic layer of the photoanode.

To verify that the presence of Fe₃O nodes is crucial for the photocatalysis observed, we have conducted the control i-t

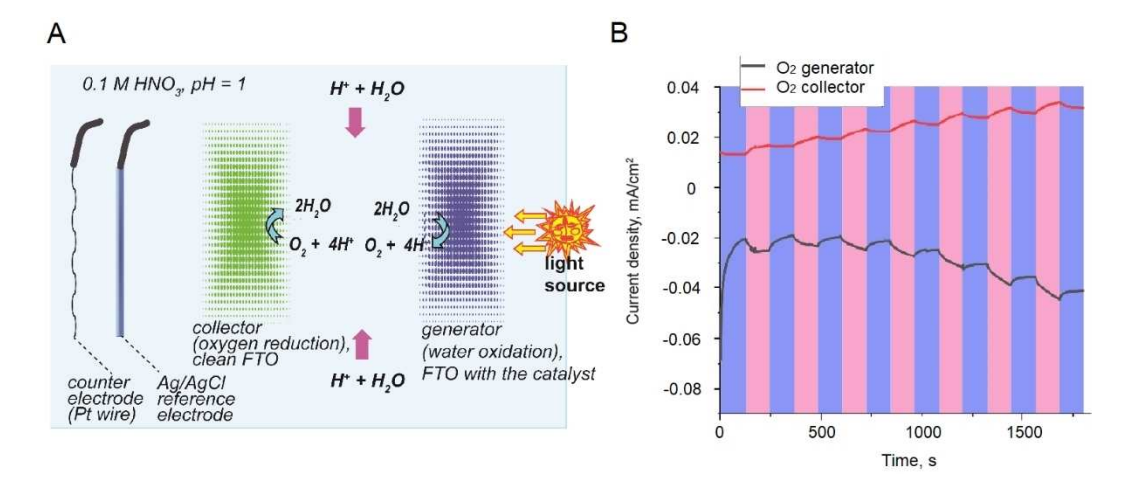


Figure 6. (A) Scheme of the generator-collector cell with water oxidation/oxygen reduction compartment of MOF-4(DC) on FTO photoanode (blue) and blank FTO cathode (green), Ag/AgCl reference electrode, and Pt wire as the auxiliary electrode. +1.4 V vs. Ag/AgCl potential was applied to the system in 0.1 M HNO₃. (B) Currents due to collection and generation of oxygen by MOF-4. The colors blue (light off) and red (light on) indicate illumination.

Chemistry Europe

European Chemical Societies Publishing

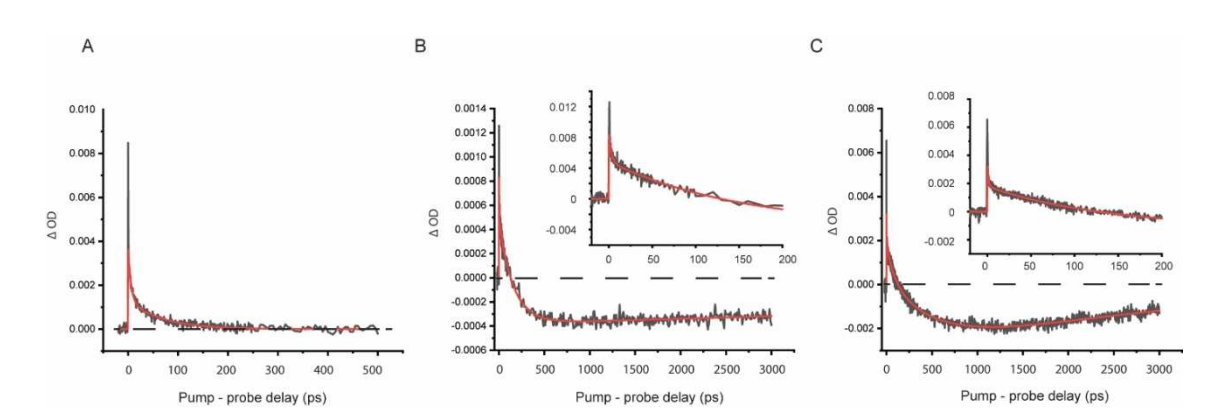


Figure 7. Optical transient absorption spectra collected at 550 nm following the sample excitation with pulse of light at 400 nm (pump) for Fe₃O acetate node in acetonitrile (A), Fe MIL-126 MOF (B) and its Ru doped analogue MOF-2 (C) suspensions in acetonitrile.

Fe MIL-126

MOF-2

measurements with UIO-67-dcbpy MOF doped with [Ru-(bpy)(dcbpy)(H_2O) $_2$] $^{2+}$ on FTO as a photoanode. $^{[14c,17b]}$ The latter has a similar linker environment (dcbpy linkers) and the same WOC in 1:12 ratio to the linker, but its Zr₆O₄(OH)₄ oxocluster can be photoactivated only under UV light, due to large bandgap of oxozirconium moieties (> 3.7 eV).[39] Electrocatalytic current generated by UIO-67-dcbpy-Ru-bpy photoanodes was significantly weaker than produced by photoanode bearing Febased analogue MOF-4 (Figure S17). ICP MS of the Ru-doped UIO-67-dcbpy confirmed 0.14 μmol/1 mg of the catalyst content that is comparable to 0.17 µmol/1 mg of MOF-4. Thus, different photo-response of these MOFs with similar Ru content correlates with different photoactivity of their metal clusters and indicates that the photoexcitation of the Fe₃O nodes is a main driving force of photoelectrocatalytic activity of Fe-based MOFs.

Optical pump-probe

To follow the light induced dynamic in MOFs, the fs optical pump-probe (OPP) experiments were conducted (Figure 7). Previously formation of the light induced charge separated states has been reported for Fe MIL-100 MOF using X-ray absorption spectroscopy while solutions of Fe₃O μ-oxo nodes were probed by optical pump-probe. [36,40] Here we compared OPP of acetate ligated Fe₃O μ-oxoclusters ([Fe₃O- $(OAc)_6(H_2O)_3]OAc$ where Ac = acetate) with Fe MIL-126 MOF and its Ru-doped analogue MOF-2. To the best of our knowledge, previous efforts to measure photo-response in suspensions of MOF crystals using OPP where not productive because of light scattering. We attempted to overcome this limitation applying OPP to the suspension of MOF microcrystals (Figure 7).

Excitation of acetate ligated Fe₃O μ-oxoclusters (Fe₃Onodes) in solution with short laser pulse at 400 nm (Figure 7A) induces transient absorption difference signal at 550 nm that can be fitted with two kinetic decay components with 5.5 ps and 68 ps lifetimes (Table 1).

Upon excitation of Fe MIL-126 MOF microcrystals, a transient absorption difference signal appears which can also

Table 1. Decay times, in ps, and relative amplitudes of decay components (in brackets) determined in optical pump-probe experiment. τ_1 (A) τ_2 (A) τ_3 (A) τ_4 (A) $[Fe_3O(OAc)_6(H_2O)_3]OAc$ 5.51 67.50 (0.54)(1)

148.97

(2.31)

88.99

(0.85)

16163.9

(-0.99)

572.28

(2.35)

2558.74

(-2.20)

2.78

1.14

(1)

(1)

be described by two kinetic decay components with 2.8 ps and 149 ps lifetimes. A long-lived (around 16 ns) bleaching is only detectable in Fe MIL-126 (Figure 7B). Presence of Ru complex in MOF (MOF-2 sample) shortens the lifetime of the bleached state from about 16 ns to around 2.6 ns (Figure 7C, Table 1). This might reflect the electron transfer between the Fe-based node and the Ru catalytic center. Nanosecond lifetimes are approximate since the setup is only capable to measure up to 3 ns delays. However, all collected data show the same trend of faster recovery of the ns state when Ru complex is integrated in the MOF. Fe MIL-126 data are in a good agreement with reported earlier time resolved XAS on Fe MIL100^[36a] indicating a light-induced state with long life time is not observable for isolated Fe₃O nodes.

DFT calculation of MOF band structure

Earlier use of Fe-MIL systems in photocatalysis [17c,23,41] and data obtained here indicate that Fe₃O nodes in MOF are photoactive and can undergo a visible-light-induced charge separation. To back this hypothesis, we conducted DFT band structure calculations for Fe with MIL-126 structure with dcbpy linkers (see Experimental Section). Such structure is possible for the linker-mixed Fe bpdc:dcbpy 1:1 MOF whose Ru-doped derivative MOF-3 showed high activity. Initial unit structures were taken from the Cambridge database deposition (Figure 8A).[24a] The geometry was optimized in the high-spin state using PBESol without relaxing the unit cell. The Hubbard U correction was added to single-point calculations performed in the



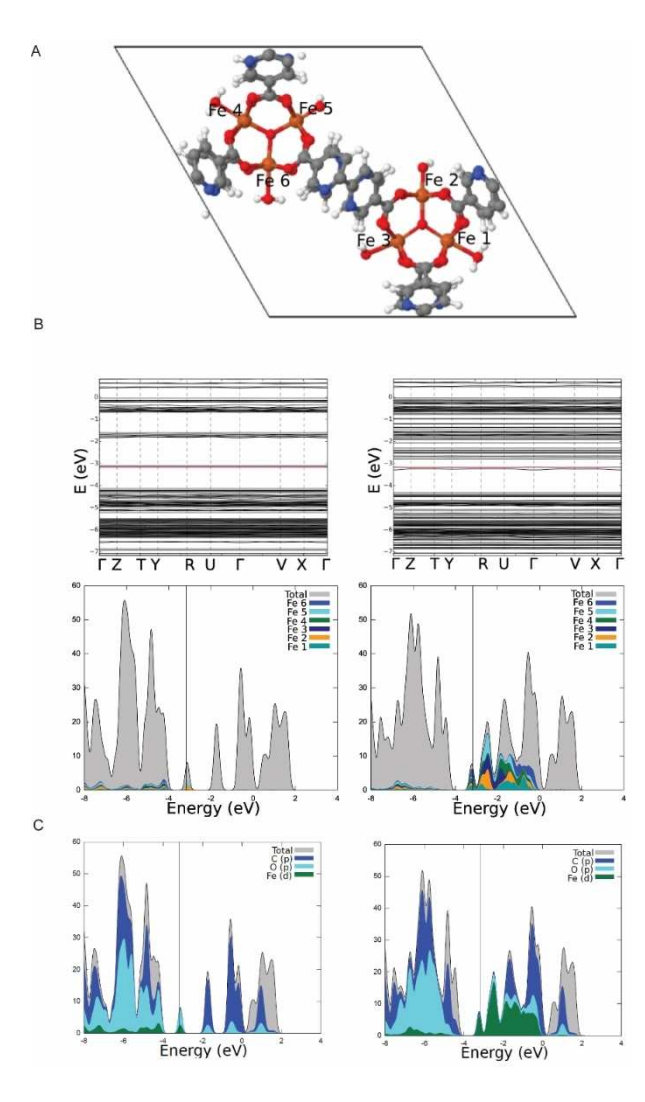


Figure 8. (A) Unit cell of Fe MIL-126 with dcbpy linker with labeling of Fe atoms 1–6. (B) Band structure and density of states for the ferromagnetically coupled state. The horizonal red line and vertical black line indicate the Fermi level. (C) Electron density localized in the d-orbitals of the six Fe atoms and the p-orbitals of the O and C atoms.

ferromagnetic spin state (Figure 8B), along with 3 antiferromagnetically coupled states (Figure S19), while allowing the spindensity to relax. The Hubbard U parameter values for iron atoms 1–6 used in our computations were 3.0, 4.5, 3.0, 3.0, 4.5, and 3.0, where the atoms are labeled as indicated in Figure 8A. Because the iron atoms come in two groups of three, only the four magnetic states where the two groups have identical alignment were considered in our calculations. The energy of these four states is given in Table 2, with the lowest energy

Table 2. Energy of different magnetic states relative to the ferromagnetic state.								
Mag. Alignment	††† , †††	↑↑↓ , ↑↑↓	$\uparrow\downarrow\uparrow$, $\uparrow\downarrow\uparrow$	↓↑↑,↓↑↑				
Relative E [eV]	0.000	-0.634	-0.544	-0.633				

state highlighted in bold. All three antiferromagnetic states are relatively close in energy, but more than 0.5 eV below the ferromagnetic state. Because optical excitations typically do not flip electron spins, we report band structures, band gaps, and densities of states separately for the two spin channels. The ferromagnetic state has a small bandgap of 0.0015 eV in the spin-down channel, and therefore, it may be possible to obtain some small conductivity in this state. The lower energy, antiferromagnetic states have band gaps between approximately 0.74-1.7 eV, corresponding to potential optical excitations at between 723-1667 nm (Table 3). Band structures and densities of states are given in Figures 8B, C, and S19. The antiferromagnetic states all have one or two flat bands just below the Fermi-level at around -3 eV. There is a large gap between this band and the remainder of the valence band, which begins around -4 eV. Table 4 lists the energies required to promote electrons from the top of these lower bands into the conduction band, which is possible with visible wavelength excitations between approximately 630-750 nm. The density of states plots in Figures 8B, S19 contains the total density of states (in gray), as well as stacked area plots of its projection onto the Fe atom d-orbitals. Together, the electron density localized in the d-orbitals of the six Fe atoms and the p-orbitals of the O and C atoms accounts for nearly the entire density of states at or directly above the Fermi-level (Figure 8C). Although the exact distribution of electron density between these sets of orbitals depends on the magnetization of the system and spin channel, any optical excitations will necessarily involve these three sets of orbitals. Optical transitions between orbitals of the same angular momentum are forbidden when the two orbitals are localized at the same site and weak otherwise. Therefore, we expect $p \rightarrow p$ optical transitions to be either rare or nonexistent, and the strongest optical excitations should involve both the d-orbitals of the Fe atoms and the p-orbitals of the other atoms.

Discussion

Development of electrocatalysts capable of splitting water upon light activation is scientifically and technologically challenging. A few MOFs were reported to split water photochemically at moderate pH, but their exact mechanisms remain largely unknown.[17c,23] Light-induced MOF-promoted water oxidation can be analyzed as multistep process, similar to the processes in natural photosynthesis.[42] Depending on the system, the first step includes incident photon absorption by either organic linker followed by linker to cluster charge transfer (LCCT such as transition in terephthalic Fe-based MOFs) or light absorption by metal-oxo clusters, with formation of an electron-hole pair if the band energy is lower than the energy of the photon (Figure 9). Following light absorption, an electron-hole charge separation is possible, and the resulting charge-separated states can be utilized for chemical transformations or collected at an electrode. Charge recombination is a competing process. It was shown previously that in some Fe-MIL MOFs, charge recombination is slowed down to micro-



Table 3. Band gap for spin-up and spin-down electrons in different magnetic states.							
Magnetic alignment	Spin up gap		Spin down gap				
	[eV]	[nm]	[eV]	[nm]			
↑↑↓,↑↑↓	0.744	1666.5	1.678	738.8			
↑↓↑,↑↓↑	1.139	1088.4	0.440	2816.4			
↓↑↑, ↓↑↑	0.778	1594.4	1.713	723.8			
<u> </u>	0.979	1266.4	0.0015	826561.3			
L							

Table 4. Excitation energy conduction band.	, to	move	electrons	below	−4 eV	into	the
		Sp	oin up				
Magnetic alignment		[e'	V]		[nm]		
↑↑↓ , ↑↑↓		1.	645		753.6		
		1.	043		755.0		
$\uparrow\downarrow\uparrow$, $\uparrow\downarrow\uparrow$		1.3	704		727.5		
↓↑↑,↓↑↑		1.9	960		632.6		

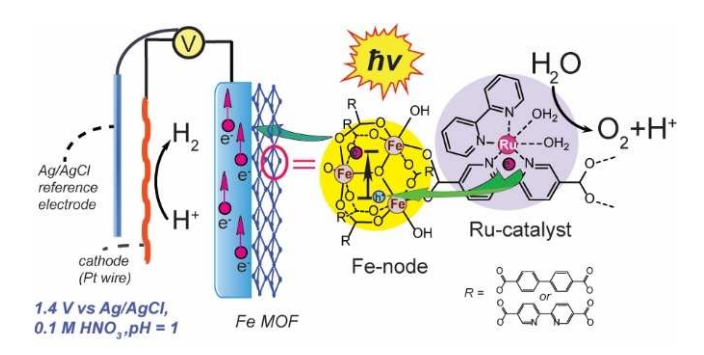


Figure 9. Proposed mechanism of the light-induced WOR during electrocatalysis with Ru-doped Fe-MOFs.

seconds, in comparison to the molecular analogues of nodes. Optical pump-probe conducted here detected similar phenomena of optically distinct state with around ns life time in MOF.

Here, we report Fe-based MOFs doped with [Ru-(bpy)(dcbpy)(H₂O)₂]²⁺ catalytic centers (Figure 1, MOFs 1–4) active in chemical and photoelectrochemical water oxidation processes at pH=1. In the previous reports, Fe-based MOFs active in photochemical WOR were shown to work at moderate pH with Ru-based photosensitizer combined with an electron acceptor [Ru(bpy)₃]²⁺ with persulfate or with an external electron acceptor (AgNO₃).^[17c,23] Replacement of benzene moiety with bipyridine ligand enables the development of the chelating framework capable of binding transition metal coordination compounds.^[17b,e,24a,30c,43] Such immobilization of active WOC can significantly increase the catalytic activity of the MOF. For instance, none of previously described Fe-MIL MOFs can catalyze WOR at acidic pH. We have found that [Ru-

(bpy)(dcbpy)(H₂O)₂]²⁺ catalytic unit can be easily introduced to the Fe-based MOFs either by linker exchange or doping by catalytic precursor [Ru(bpy)(cymene)]Cl₂. These doping procedures are intended to achieve a photocatalytic response of the assembly in WOR due to the electron transfer from the immobilized Ru-WOC to the light-activated Fe₃O nodes of the MOF. This should allow the photogenerated holes to promote WOR while electrons are collected at the anode (Figure 9). Electrode-immobilized materials combining a photosensitizer and Ru-based WOC were reported earlier, but these were only active at moderate pH. [24b,44] This is due to a fixed + 1.23 V redox potential of broadly used [Ru(bpy)₃]²⁺ photosensitizer, which is insufficient to drive most WOCs in acid. Photoactive WOC Fe₂O₃, featuring the highly oxidizing approximately +2.3 V holes, is not stable at low pH. The role of Fe MOF structural units, namely Fe₃O nodes in photoelectrochemical WOR was assessed by following: 1) DFT calculation of the bandgap for Fe MIL-126 with dcbpy linker; 2) Kubelka-Munk analysis of diffuse reflectance spectra to obtain bandgap energies for the pristine MOFs; 3) comparison to the MOF with non-Fe nodes, namely UIO-67 with Zr₆ oxocluster lacking photosensitivity to visible light; 4) fsps optical pump-probe. Obtained results are in agreement with each other and confirm that Fe₃O nodes are susceptible to the visible light and able to generate the charge separated states upon illumination. Subsequent electron transfer from the Rucatalytic center to the electron vacancies (holes) in the Fe₃O nodes promotes water splitting. Relatively low photoresponse of Ru-doped UIO-67-dcbpy indicates that [Ru(bpy)(dcbpy)] moiety in Ru-doped MOF cannot be considered as a photoactive "light antenna" capable of driving photoelectrochemical water splitting. [45] Rull complexes known for their bright colors due to metal to ligand charge transfer (MLCT) transitions become quickly oxidized under WOC conditions to weakly colored Ru^{III} and Ru^{IV} states, thus, losing their ability to interact with light. Instead, our light-induced experiments show that light-activated µ₃-oxo bridged Fe₃O nodes cause water oxidation catalysis, likely due to the highly oxidizing potential of the generated holes. [27,36a] DFT calculations show that Fe₃O based dd transitions are low in energy and overlap with visible light absorption window. DFT results for the Fe MOF confirm the presence of relatively low energy (<2 eV) bandgap in Fe₃O nodes of the MOF that leads to the formation of charge separated states under visible light. This intensifies Ru-based water oxidation catalysis in the MOFs where similar Fe₃O nodes



are in close proximity with [Ru(bpy)(dcbpy)(H₂O)₂]²⁺ catalytic centers. The use of MOFs for light absorption, energy and charge transfer and catalysis is currently emerging and multiple structural factors can affect material performance. Improvement of the photocatalytic properties for structurally interpenetrated MOFs was noted previously. [46] Internal photocatalytic durability and better electron transfer in these MOFs can be attributed to closer interframework distances accelerating interaction between reactive species within the framework.[47] Thus, interpenetrated topology of the Fe MIL-126 (MOF-1, MOF-2 and MOF-3) may be beneficial to their photoelectrochemical performance, via facilitation of Ru-catalyst to Fe₃O-node electron transfer. Further development is possible via MOF's linker modification for enhanced light absorption, electrical conductivity, lowering the MOF solubility in acid, and Ru-ligand modification for faster WOC catalysis or WOC substitution to 3rd row (3d) metal-based system. Our findings give further insight into development of light-driven water-splitting systems based on Earth-abundant metals.

Conclusions

We reported the synthesis, characterization, electro- and photoelectrocatalytic performance of a new water splitting material consisting of iron-based metal-organic frameworks (MOFs) (Fe MIL-126 and Fe MOF-dcbpy) doped with catalytically competent [Ru(bpy)(dcbpy)(H₂O)₂]²⁺complex (bpy = 2,2'-bipyridine, dcbpy = 2,2'-bipyridine-5,5'-dicarboxylate). To date, there are no MOF-based electrocatalysts capable of photoactivation in acidic media. In our research, we have found that Fe-based MOFs doped with [Ru(bpy)(dcbpy)(H₂O)₂]²⁺and drop-casted on fluorine-doped tin oxide (FTO) glass electrode exhibit long-term stability (>8 h) in electrocatalytic water oxidation at pH=1with visible light induced catalytic current enhancement exceeding one order of magnitude. This can be attributed to a charge transfer from Ru catalytic center to the photoinduced holes of Fe₃O nodes of the MOFs. The role of Fe₃O nodes in photoelectrochemical water oxidation reaction (WOR) was confirmed using density functional theory (DFT) calculation, diffuse reflectance spectra comparison with MOFs having different oxo-nodes (Fe- and Zr-based) and fs-ps optical pump-probe. Study of this photoactive material is important for better understanding of photochemical processes in MOFs and provides further insight for development of the catalytic systems toward sustainable hydrogen production, via the approach of artificial photosynthesis.

Experimental Section

Materials

All chemicals and solvents were purchased from Sigma Aldrich, AK Scientific, and TCI America, and they were used as received. Nuclear magnetic resonance (NMR) spectra were recorded on a Bruker AV-III-HD-400 400 MHz spectrometer, and chemical shifts were referenced to solvent residual peaks. Aqueous solutions were prepared

using ultrapure (Type 1) water (resistivity 18.2 M Ω -cm at 25 °C) from Q-POD unit of Milli-Q integral water purification system (Millipore, Billerica, MA, USA). PXRD data were collected using Panalytical Empyrean Powder X-ray diffractometer. All SEM imaging was undertaken on a Zeiss EVO LS15 SEM using 5 kV accelerating voltage, a probe current of 15–40 pA and working distance 8–15 mm. Diffuse reflectance spectra were recorded using Lambda 950 UV-Vis spectrophotometer.

Fabrication of MOF thin films on FTO electrode surface

Growing of MOF thin films (GR-electrodes) was performed according to the procedures described for UIO-67 MOF^[16c,17a,27,48] on the bpdc self-assembled monolayer (SAM) preliminary formed on a clean FTO surface. Doping of MOF thin films on FTO with Rucatalysts proceeded depending on the MOF type: by on-MOF synthesis for MOF-4 thin film and by postsynthetic exchange in water for MOF-1 thin film electrodes. On-MOF thin film synthesis was accomplished by heating of FTO glass electrodes with MOF-4 thin film grown on bpdc SAM in solution of the catalyst precursor–Ru(cymene)bpyCl₂ in dimethylformamide (DMF) at 130 °C for 12 h, stirred. For MOF-1 thin film electrodes, doping was realized using bpdc MOF ligand postsynthetic exchange with dcbpy moiety of [Ru(bpy)(dcbpy)(H₂O)₂]Cl₂ solution in water at r.t. overnight.^[27]

Photoelectrode fabrication using drop casting of catalytically active MOFs (DC-electrodes) was performed according to the reported procedure. [17c] For each electrode, 4 mg of MOF was suspended in 0.5 mL of isopropanol with addition of 8 µL of Nafion solution (5% in alcohol/water, Sigma Aldrich Inc.). Second, the suspended mixture obtained was layered on an electrode surface, and we waited until almost complete evaporation of isopropanol to deposit another layer. Five layers of the suspended MOF mixture were deposited. After drop casting, the MOF-bearing electrodes were dried on air at r. t.

Electrochemistry

Cyclic voltammetry was accomplished using a potentiostat (CHI 627 C; CH Instruments Inc., Austin, TX, USA) using standard single-compartment 3-electrode cell. The FTO electrodes were electrically contacted using the uncoated FTO layer and masked to a geometrical surface area of 1 cm². A piece of a platinum wire served as the counter electrode, and a saturated Ag/AgCl electrode served as the reference electrode. Anodes were illuminated with unfocused 500 W light source at ~25 cm away from the sample passed through UV-filter/IR filter (~ 2 cm of CuSO₄ water solution).

All reported measurements were repeated several times to ensure the reproducibility of results.

ICP-MS

For Ru and Fe loading, determination Element 2TM ICP-MS system was used. The Ru-doped MOF samples were digested in 70% ultrahigh purity nitric acid (Seastar Chemicals) at 90 °C for 12 h. The solution was then diluted 35 times with water and purified by filtration trough a 0.2 μm syringe-filter. Further dilutions were performed with 2% ultrapure nitric acid.

Resonance Raman spectroscopy

An XploRA Raman microscope from HORIBA was used for Raman measurements. The software was LabSpec5. The excitation wavelength was 532 nm with 0.10 mW power. A grating with 1800 g/ $\,$



mm dispersed the scattered Raman signal. A 50 X objective was mounted on the microscope. The slit was open for 0.200 mm and an approximate resolution of about 7 cm⁻¹ was achieved. The data were collected by averaging 100 scans, and each scan exposure time was 1 sec.

FTIR spectroscopy

A Thermo Nicolet Nexus FTIR Spectrometer was used for FTIR measurements. The device was run on OMNIC software. Some of the specifications of the device were a MCT detector and a KBr beam splitter. The interior space of the spectrometer was continuously purged with nitrogen gas for at least one hour before the measurement to reduce the background from water vapor. Data collection used a small amount of the dry powder sample pressed against an attenuated total reflectance (ATR) diamond crystal by a handle, and the measurements were done at room temperature. The graph consists of 36 scans with 4 cm⁻¹ resolution.

EPR

Low-temperature X-band EPR spectra were recorded with a Bruker EMX X-band spectrometer equipped with an X-band CW microwave bridge. The sample temperature was maintained at 20 K using a ColdEdge closed cycle cryostat. The standard EPR sample tubes were filled with MOF suspension in acid through all of the resonator space.

XAS and EXAFS measurements

X-ray absorption spectra were collected at the Advanced Photon Source (APS) at Argonne National Laboratory on bending magnet beamline 20 at electron energy 23 keV and average current of 100 mA. The radiation was monochromatized by a Si(110) crystal monochromator. The intensity of the X-rays was monitored by three ion chambers (I_0 , I_1 , and I_2) and placed before the sample (I_0) and after the sample (I_1 and I_2). I_1 , I_2 and I_3 were filled with 100% nitrogen. Fe or Ru metal foils was placed between the I₂ and I₃, and its absorption was recorded with each scan for energy calibration. The X-ray energy was calibrated by setting the first maximum in the derivative of the Fe or Ru metals K-edge XANES spectrum to 7112 eV or 22117 eV correspondingly. For XAS analysis of reactive intermediates plastic (Lexan) EXAFS sample holders (inner dimensions of 12 mm×2 mm×3 mm) filled with frozen solutions were inserted into a cryostat pre-cooled to 20 K. The samples were kept at 20 K in a He atmosphere at ambient pressure. Data were recorded as fluorescence excitation spectra using a 13-element energy-resolving detector. In order to reduce the risk of sample damage by X-ray defocused mode (beam size 1×7 mm) was used and no damage was observed. The shutter was synchronized with the scan software preventing exposure to X-rays between scans and during spectrometer movements.

Ultrafast time-resolved optical spectroscopy (optical pump-probe)

The home-built optical pump-probe spectroscopy system ^[49] was used to measure acetate ligated Fe₃O μ -oxoclusters ([Fe₃O-(OAc) $_6$ (H₂O) $_3$]OAc where Ac=acetate) solutions and Fe MIL-126 MOF and its Ru-doped analogue MOF-2 suspensions in acetonitrile (around 0.1 mg/1 mL). Briefly, the output from a home-built self-mode-locked Ti-sapphire laser was amplified at 1 kHz repetition rate in a regenerative amplifier, resulting in about 100 fs long 0.4 mJ light pulses centered at around 790 nm. A nonlinear crystal

(BBO) was used to generate second harmonic pulses centered at about 400 nm. The latter pulses were used to pump the sample. The pump-induced transient absorption of a sample was probed with broadband femtosecond continuum pulses generated in a sapphire plate using a fraction of the amplifier output. A fraction of continuum pulse was used as a reference beam. After passing through sample, probe wavelength of interest was selected by an Oriel MS257 imaging monochromator and intensities of probe and reference beams were detected by home-built amplified photodiodes and analyzed by a PC computer. Temporal resolution of the system was defined by cross-correlations between pump and probe pulses and was typically around 300 fs. All experiments were performed at room temperature. Fe MIL-126 MOF microcrystals were suspended in acetonitrile by sonification for 5 minutes prior to the OPP experiment. Same data were obtained by using suspension of Fe MIL-126 microcrystals grown for just 2 h and for suspensions of regular Fe MIL-126 preparations where large size crystals were allowed to settle down by brief centrifugation while supernatant was collected for OPP experiment.

DFT calculations

DFT was carried out in Quantum Espresso^[50] on a 3x3x3 k-point grid, using rrkjus ultrasoft pseudopotentials from pslibrary,^[51] with a kinetic energy cutoff of 50 Ry and a charge-density cutoff of 350 Ry. Because local and semi-local density functionals tend to over-delocalize electrons, a Hubbard U correction^[52] was added to the PBESol functional^[53] to model onsite exchange interactions between the Fe d-orbital electrons. The Hubbard U parameter was computed in Quantum Espresso's, using linear-response theory^[54] and rounded to the nearest 0.5.

Acknowledgements

This research was supported by NSF, CHE-2155060 (Y.P.). Optical pump-probe experiments were supported by the U.S. Department of Energy, Office of Basic Energy Sciences (Grant DE-SC0018239 to S.S.). The use of the Advanced Photon Source, an Office of Science User Facility operated by the U.S. Department of Energy (DOE) Office of Science by Argonne National Laboratory, was supported by the U.S. DOE under Contract DE-AC02-06CH11357. The PNC/ XSD (Sector 20) facilities at the Advanced Photon Source and research at these facilities were supported by the U.S. Department of Energy, Basic Energy Science and the Canadian Light Source. Access to EPR was provided by the Amy Instrumentation Facility, Department of Chemistry, under the supervision of Dr. Michael Everly. We thank Prof. L. Rokhinson from Purdue University for providing access to Zeiss EVO LS15 electron microscope. We thank Winter R. Allen, Gabriel Bury and Ananthesh Sundaresh of Purdue University for assistance with resonance Raman, EPR and SEM measurements.

Conflict of Interest

The authors declare no conflict of interest.

Data Availability Statement

The data that support the findings of this study are available in the supplementary material of this article.

Keywords: Fe $_3$ O nodes \cdot metal-organic frameworks \cdot photoanode \cdot ruthenium-based water oxidation catalyst \cdot water splitting

- a) I. Roger, M. A. Shipman, M. D. Symes, Nat. Chem. Rev. 2017, 1, 0003;
 b) M. Kondo, H. Tatewaki, S. Masaoka, Chem. Soc. Rev. 2021, 50, 6790–6831;
 c) R. Ezhov, A. K. Ravari, Y. Pushkar, Angew. Chem. Int. Ed. 2020, 59, 13502–13505;
 Angew. Chem. 2020, 132, 13604–13607;
 d) J. D. Blakemore, R. H. Crabtree, G. W. Brudvig, Chem. Rev. 2015, 115, 12974–13005.
- [2] M. Carmo, D. L. Fritz, J. Mergel, D. Stolten, Int. J. Hydrogen Energy 2013, 38, 4901–4934.
- [3] a) S. Anantharaj, V. Aravindan, Adv. Energy Mater. 2020, 10, 1902666;
 b) Z. Lei, T. Wang, B. Zhao, W. Cai, Y. Liu, S. Jiao, Q. Li, R. Cao, M. Liu, Adv. Energy Mater. 2020, 10, 2000478.
- [4] J. T. Arens, M. Blasco-Ahicart, K. Azmani, J. Soriano-López, A. García-Eguizábal, J. M. Poblet, J. R. Galan-Mascaros, J. Catal. 2020, 389, 345–351.
- [5] a) C. Spöri, J. T. H. Kwan, A. Bonakdarpour, D. P. Wilkinson, P. Strasser, Angew. Chem. Int. Ed. 2017, 56, 5994–6021; Angew. Chem. 2017, 129, 6088–6117; b) C. C. McCrory, S. Jung, I. M. Ferrer, S. M. Chatman, J. C. Peters, T. F. Jaramillo, J. Am. Chem. Soc. 2015, 137, 4347–4357; c) Y. Yao, S. Hu, W. Chen, Z.-Q. Huang, W. Wei, T. Yao, R. Liu, K. Zang, X. Wang, G. Wu, W. Yuan, T. Yuan, B. Zhu, W. Liu, Z. Li, D. He, Z. Xue, Y. Wang, X. Zheng, J. Dong, C.-R. Chang, Y. Chen, X. Hong, J. Luo, S. Wei, W.-X. Li, P. Strasser, Y. Wu, Y. Li, Nat. Catal. 2019, 2, 304–313.
- [6] a) Y. Lee, J. Suntivich, K. J. May, E. E. Perry, Y. Shao-Horn, J. Phys. Chem. Lett. 2012, 3, 399–404; b) M. J. Kirshenbaum, M. H. Richter, M. Dasog, ChemCatChem 2019, 11, 3877–3881.
- [7] a) A. Fujishima, K. Honda, Nature 1972, 238, 37–38; b) I. M. Szilágyi, B. Fórizs, O. Rosseler, Á. Szegedi, P. Németh, P. Király, G. Tárkányi, B. Vajna, K. Varga-Josepovits, K. László, A. L. Tóth, P. Baranyai, M. Leskelä, J. Catal. 2012, 294, 119–127; c) M. Mishra, D.-M. Chun, Appl. Cat. A Gen. 2015, 498, 126–141; d) C. Karunakaran, S. Senthilvelan, Electrochem. Commun. 2006, 8, 95–101; e) B. J. Trześniewski, W. A. Smith, J. Mater. Chem. A 2016, 4, 2919–2926; f) X. Du, Y. Ding, F. Song, B. Ma, J. Zhao, J. Song, Chem. Commun. 2015, 51, 13925–13928.
- [8] a) D. Primc, M. Bärtsch, D. Barreca, G. Carraro, C. Maccato, C. Sada, M. Niederberger, Sustain. Energy Fuels 2017, 1, 199–206; b) S. Kment, F. Riboni, S. Pausova, L. Wang, L. Wang, H. Han, Z. Hubicka, J. Krysa, P. Schmuki, R. Zboril, Chem. Soc. Rev. 2017, 46, 3716–3769; c) S. Piskunov, O. Lisovski, J. Begens, D. Bocharov, Y. F. Zhukovskii, M. Wessel, E. Spohr, J. Phys. Chem. C 2015, 119, 18686–18696.
- [9] Y. Li, H. Xu, S. Ouyang, J. Ye, Phys. Chem. Chem. Phys. 2016, 18, 7563–7572.
- [10] a) M. Bendova, F. Gispert-Guirado, A. W. Hassel, E. Llobet, A. Mozalev, Nano Energy 2017, 33, 72–87; b) L. K. Preethi, R. P. Antony, T. Mathews, L. Walczak, C. S. Gopinath, Sci. Rep. 2017, 7, 14314.
- [11] a) A. Jelinska, K. Bienkowski, M. Jadwiszczak, M. Pisarek, M. Strawski, D. Kurzydlowski, R. Solarska, J. Augustynski, ACS Catal. 2018, 8, 10573–10580; b) K. Hideki, H. Mikihiro, K. Ryoko, S. Yoshiki, K. Akihiko, Chem. Lett. 2004, 33, 1348–1349; c) H. Wang, T. Deutsch, J. A. Turner, J. Electrochem. Soc. 2008, 155, F91.
- [12] J. Krysa, M. Zlamal, S. Kment, M. Brunclikova, Z. Hubicka, *Molecules* 2015, 20, 1046–1058.
- [13] a) S. Mine, Z. Lionet, H. Shigemitsu, T. Toyao, T.-H. Kim, Y. Horiuchi, S. W. Lee, M. Matsuoka, Res. Chem. Intermed. 2020, 46, 2003–2015; b) W. Gao, J. Lu, S. Zhang, X. Zhang, Z. Wang, W. Qin, J. Wang, W. Zhou, H. Liu, Y. Sang, Adv. Sci. 2019, 6, 1901244; c) K. G. M. Laurier, F. Vermoortele, R. Ameloot, D. E. De Vos, J. Hofkens, M. B. J. Roeffaers, J. Am. Chem. Soc. 2013, 135, 14488–14491.
- [14] a) A. Dhakshinamoorthy, Z. Li, H. Garcia, Chem. Soc. Rev. 2018, 47, 8134–8172; b) J.-D. Xiao, H.-L. Jiang, Acc. Chem. Res. 2019, 52, 356–366; c) C. Wang, Z. Xie, K. E. deKrafft, W. Lin, J. Am. Chem. Soc. 2011, 133, 13445–13454; d) W. Wang, X. Xu, W. Zhou, Z. Shao, Adv. Sci. 2017, 4, 1600371.
- [15] a) S. M. Cohen, Chem. Rev. 2012, 112, 970–1000; b) S. M. Cohen, J. Am. Chem. Soc. 2017, 139, 2855–2863; c) R. J. Marshall, C. T. Lennon, A. Tao,

- H. M. Senn, C. Wilson, D. Fairen-Jimenez, R. S. Forgan, *J. Mater. Chem. A* **2018**, *6*, 1181–1187; d) T. Zhang, K. Manna, W. Lin, *J. Am. Chem. Soc.* **2016**, *138*, 3241–3249; e) E. D. Bloch, D. Britt, C. Lee, C. J. Doonan, F. J. Uribe-Romo, H. Furukawa, J. R. Long, O. M. Yaghi, *J. Am. Chem. Soc.* **2010**, *132*, 14382–14384.
- [16] a) J. Yang, D. Wang, H. Han, C. Li, Acc. Chem. Res. 2013, 46, 1900–1909;
 b) H. Zhu, D. Liu, D. Zou, J. Zhang, J. Mater. Chem. A 2018, 6, 6130–6154;
 c) S. Lin, Y. Pineda-Galvan, W. A. Maza, C. C. Epley, J. Zhu, M. C. Kessinger, Y. Pushkar, A. J. Morris, ChemSusChem 2017, 10, 514–522.
- [17] a) S. Y. Lin, A. K. Ravari, J. Zhu, P. M. Usov, M. Cai, S. R. Ahrenholtz, Y. Pushkar, A. J. Morris, ChemSusChem 2018, 11, 464–471; b) W. A. Maza, A. J. Morris, J. Phys. Chem. C 2014, 118, 8803–8817; c) Y. Horiuchi, T. Toyao, K. Miyahara, L. Zakary, D. D. Van, Y. Kamata, T.-H. Kim, S. W. Lee, M. Matsuoka, Chem. Commun. 2016, 52, 5190–5193; d) R. Ezhov, A. Karbakhsh Ravari, A. Page, Y. Pushkar, ACS Catal. 2020, 10, 5299–5308; e) G. Nickerl, M. Leistner, S. Helten, V. Bon, I. Senkovska, S. Kaskel, Inorg. Chem. Front. 2014, 1, 325–330; f) D. Lebedev, R. Ezhov, J. Heras-Domingo, A. Comas-Vives, N. Kaeffer, M. Willinger, X. Solans-Monfort, X. Huang, Y. Pushkar, C. Copéret, ACS Cent. Sci. 2020, 6, 1189–1198; g) T. Toyao, M. Saito, S. Dohshi, K. Mochizuki, M. Iwata, H. Higashimura, Y. Horiuchi, M. Matsuoka, Chem. Commun. 2014, 50, 6779–6781; h) X. Liang, S. Yang, J. Yang, W. Sun, X. Li, B. Ma, J. Huang, J. Zhang, L. Duan, Y. Ding, Appl. Catal. B 2021, 291, 120070; i) C. Wang, J. L. Wang, W. Lin, J. Am. Chem. Soc. 2012, 134, 19895–19908.
- [18] a) S. Pullen, S. Ott, *Top. Catal.* 2016, 59, 1712–1721; b) M. B. Majewski, A. W. Peters, M. R. Wasielewski, J. T. Hupp, O. K. Farha, *ACS Energy Lett.* 2018, 3, 598–611; c) M. A. Nasalevich, C. H. Hendon, J. G. Santaclara, K. Svane, B. van der Linden, S. L. Veber, M. V. Fedin, A. J. Houtepen, M. A. van der Veen, F. Kapteijn, A. Walsh, J. Gascon, *Sci. Rep.* 2016, 6, 23676; d) M. A. Nasalevich, M. van der Veen, F. Kapteijn, J. Gascon, *CrystEng-Comm* 2014, 16, 4919–4926.
- [19] T. Musho, J. Li, N. Wu, Phys. Chem. Chem. Phys. 2014, 16, 23646–23653.[20] M. C. Lawrence, C. Schneider, M. J. Katz, Chem. Commun. 2016, 52,

4971-4974.

- [21] a) P. Horcajada, F. Salles, S. Wuttke, T. Devic, D. Heurtaux, G. Maurin, A. Vimont, M. Daturi, O. David, E. Magnier, N. Stock, Y. Filinchuk, D. Popov, C. Riekel, G. Férey, C. Serre, J. Am. Chem. Soc. 2011, 133, 17839–17847; b) X. Liu, Y. Zhou, L. Tang, L. Luo, G. Zeng, ACS Appl. Mater. Interfaces
- 2017, 9, 20255–20275.
 [22] a) X.-Y. Dao, J.-H. Guo, Y.-P. Wei, F. Guo, Y. Liu, W.-Y. Sun, *Inorg. Chem.*2019, 58, 8517–8524; b) X.-Y. Dao, J.-H. Guo, X.-Y. Zhang, S.-Q. Wang, X.-M. Cheng, W.-Y. Sun, *J. Mater. Chem. A* 2020, 8, 25850–25856.
- [23] L. Chi, Q. Xu, X. Liang, J. Wang, X. Su, Small 2016, 12, 1351-1358.
- [24] a) D. Bara, C. Wilson, M. Mörtel, M. M. Khusniyarov, S. Ling, B. Slater, S. Sproules, R. S. Forgan, J. Am. Chem. Soc. 2019, 141, 8346–8357; b) D. Wang, R. N. Sampaio, L. Troian-Gautier, S. L. Marquard, B. H. Farnum, B. D. Sherman, M. V. Sheridan, C. J. Dares, G. J. Meyer, T. J. Meyer, J. Am. Chem. Soc. 2019, 141, 7926–7933; c) S. Surblé, C. Serre, C. Mellot Draznieks, F. Millange, G. Férey, Chem. Commun. 2006, 284–286; d) M. Dan-Hardi, H. Chevreau, T. Devic, P. Horcajada, G. Maurin, G. Férey, D. Popov, C. Riekel, S. Wuttke, J.-C. Lavalley, A. Vimont, T. Boudewijns, D. de Vos, C. Serre, Chem. Mater. 2012, 24, 2486–2492.
- [25] a) L. Shi, T. Wang, H. Zhang, K. Chang, X. Meng, H. Liu, J. Ye, Adv. Sci. 2015, 2, 1500006; b) D. Wang, Z. Li, Res. Chem. Intermed. 2017, 43, 5169–5186.
- [26] L. Peng, M. Asgari, P. Mieville, P. Schouwink, S. Bulut, D. T. Sun, Z. Zhou, P. Pattison, W. van Beek, W. L. Queen, ACS Appl. Mater. Interfaces 2017, 9, 23957–23966.
- [27] R. Ezhov, A. K. Ravari, A. Page, Y. Pushkar, ACS Catal. 2020, 10, 5299– 5308.
- [28] E. M. Thoresen, S. Øien-Ødegaard, G. Kaur, M. Tilset, K. P. Lillerud, M. Amedjkouh, RSC Adv. 2020, 10, 9052–9062.
- [29] X. Yu, S. M. Cohen, Chem. Commun. 2015, 51, 9880–9883.
- [30] a) M. I. Gonzalez, E. D. Bloch, J. A. Mason, S. J. Teat, J. R. Long, *Inorg.* 2015, 54, 2995–3005; b) K. Manna, T. Zhang, W. Lin, J. Am. Chem. Soc. 2014, 136, 6566–6569; c) H. Fei, S. M. Cohen, Chem. Commun. 2014, 50, 4810–4812.
- [31] L. S. Xie, G. Skorupskii, M. Dincă, Chem. Rev. 2020, 120, 8536-8580.
- [32] a) P. Horcajada, C. Serre, G. Maurin, N. A. Ramsahye, F. Balas, M. Vallet-Regí, M. Sebban, F. Taulelle, G. Férey, J. Am. Chem. Soc. 2008, 130, 6774–6780; b) T. Devic, P. Horcajada, C. Serre, F. Salles, G. Maurin, B. Moulin, D. Heurtaux, G. Clet, A. Vimont, J.-M. Grenèche, B. L. Ouay, F. Moreau, E. Magnier, Y. Filinchuk, J. Marrot, J.-C. Lavalley, M. Daturi, G. Férey, J. Am. Chem. Soc. 2010, 132, 1127–1136; c) J. Jiang, O. M. Yaghi, Chem. Rev. 2015, 115, 6966–6997.

- [33] V. Caballero, F. M. Bautista, J. M. Campelo, D. Luna, R. Luque, J. M. Marinas, A. A. Romero, I. Romero, M. Rodríguez, I. Serrano, J. M. Hidalgo, A. Llobet, Mol. Catal. A. Chem. 2009, 308, 41–45.
- [34] D. J. Wasylenko, C. Ganesamoorthy, B. D. Koivisto, M. A. Henderson, C. P. Berlinguette, *Inorg. Chem.* **2010**, *49*, 2202–2209.
- [35] W. A. Maza, R. Padilla, A. J. Morris, J. Am. Chem. Soc. 2015, 137, 8161–8168.
- [36] a) L. Hanna, P. Kucheryavy, C. Liu, X. Zhang, J. V. Lockard, J. Phys. Chem. C 2017, 121, 13570–13576; b) L. Hanna, P. Kucheryavy, N. Lahanas, J. V. Lockard, J. Chem. Phys. 2019, 150, 10.
- [37] A. Ferguson, L. Liu, S. J. Tapperwijn, D. Perl, F. X. Coudert, S. Van Cleuvenbergen, T. Verbiest, M. A. van der Veen, S. G. Telfer, Nat. Chem. 2016, 8, 250–257.
- [38] a) B. D. Sherman, M. V. Sheridan, C. J. Dares, T. J. Meyer, *Anal. Chem.* 2016, 88, 7076–7082; b) M. V. Sheridan, D. J. Hill, B. D. Sherman, D. Wang, S. L. Marquard, K.-R. Wee, J. F. Cahoon, T. J. Meyer, *Nano Lett.* 2017, 17, 2440–2446.
- [39] S. R. Teeparthi, E. W. Awin, R. Kumar, Sci. Rep. 2018, 8, 5541.
- [40] F. Liedy, R. Shi, M. Coletta, J. Vallejo, E. K. Brechin, G. Lefkidis, W. Hubner, J. O. Johansson, *J. Magn. Magn. Mater.* **2020**, *501*, 7.
- [41] a) C. Wang, D. Liu, W. Lin, J. Am. Chem. Soc. 2013, 135, 13222–13234;
 b) J.-L. Wang, C. Wang, W. Lin, ACS Catal. 2012, 2, 2630–2640; c) Y. Horiuchi, T. Toyao, M. Takeuchi, M. Matsuoka, M. Anpo, Phys. Chem. Chem. Phys. 2013, 15, 13243–13253.
- [42] a) W. Wang, M. O. Tadé, Z. Shao, Chem. Soc. Rev. 2015, 44, 5371–5408;
 b) J. G. Santaclara, F. Kapteijn, J. Gascon, M. A. van der Veen, CrystEng-Comm 2017, 19, 4118–4125;
 c) M. Kitano, M. Hara, J. Mater. Chem. 2010, 20, 627–641;
 d) Z. Zhang, X. Li, B. Liu, Q. Zhao, G. Chen, RSC Adv. 2016, 6, 4289–4295.
- [43] a) H. Luo, Z. Zeng, G. Zeng, C. Zhang, R. Xiao, D. Huang, C. Lai, M. Cheng, W. Wang, W. Xiong, Y. Yang, L. Qin, C. Zhou, H. Wang, Y. Zhou, S. Tian, Chem. Eng. J. 2020, 383, 123196; b) A. E. Platero-Prats, A. Bermejo Gómez, L. Samain, X. Zou, B. Martín-Matute, Chem. Eur. J. 2015, 21, 861–866.
- [44] a) M. V. Sheridan, B. D. Sherman, Z. Fang, K. Wee, M. K. Coggins, T. J. Meyer, ACS Catal. 2015, 5, 4404–4409; b) B. D. Sherman, Y. Xie, M. V.

- Sheridan, D. Wang, D.W. Shaffer, T.J. Meyer, J.J. Concepcion, ACS Energy Lett. 2017, 2, 124–128.
- [45] R. Navarro Amador, M. Carboni, D. Meyer, *RSC Adv.* **2017**, *7*, 195–200.
- [46] a) S. Zhang, L. Li, S. Zhao, Z. Sun, J. Luo, *Inorg.* 2015, 54, 8375–8379;
 b) E. A. Dolgopolova, A. M. Rice, C. R. Martin, N. B. Shustova, *Chem. Soc. Rev.* 2018, 47, 4710–4728.
- 47] Z. Xia, C. He, X. Wang, C. Duan, *Nat. Commun.* **2017**, *8*, 361.
- [48] B. A. Johnson, A. Bhunia, S. Ott, Dalton Trans. 2017, 46, 1382-1388.
- [49] S. Savikhin, W. Xu, V. Soukoulis, P. R. Chitnis, W. S. Struve, *Biophys. J.* 1999, 76, 3278–3288.
- [50] P. Giannozzi, O. Andreussi, T. Brumme, O. Bunau, M. Buongiorno Nardelli, M. Calandra, R. Car, C. Cavazzoni, D. Ceresoli, M. Cococcioni, N. Colonna, I. Carnimeo, A. Dal Corso, S. de Gironcoli, P. Delugas, R. A. DiStasio, A. Ferretti, A. Floris, G. Fratesi, G. Fugallo, R. Gebauer, U. Gerstmann, F. Giustino, T. Gorni, J. Jia, M. Kawamura, H. Y. Ko, A. Kokalj, E. Küçükbenli, M. Lazzeri, M. Marsili, N. Marzari, F. Mauri, N. L. Nguyen, H. V. Nguyen, A. Otero-de-la-Roza, L. Paulatto, S. Poncé, D. Rocca, R. Sabatini, B. Santra, M. Schlipf, A. P. Seitsonen, A. Smogunov, I. Timrov, T. Thonhauser, P. Umari, N. Vast, X. Wu, S. Baroni, J. Condens. Matter Phys. 2017, 29, 465901.
- [51] A. Dal Corso, Comput. Mater. Sci. 2014, 95, 337-350.
- [52] a) V. I. Anisimov, J. Zaanen, O. K. Andersen, *Phys. Rev. B* **1991**, *44*, 943–954; b) V. I. Anisimov, I. V. Solovyev, M. A. Korotin, M. T. Czyżyk, G. A. Sawatzky, *Phys. Rev. B* **1993**, *48*, 16929–16934; c) A. I. Liechtenstein, V. I. Anisimov, J. Zaanen, *Phys. Rev. B* **1995**, *52*, R5467-R5470.
- [53] G. I. Csonka, J. P. Perdew, A. Ruzsinszky, P. H. T. Philipsen, S. Lebègue, J. Paier, O. A. Vydrov, J. G. Ángyán, Phys. Rev. B 2009, 79, 155107.
- [54] I. Timrov, N. Marzari, M. Cococcioni, Phys. Rev. B 2018, 98, 085127.

Manuscript received: November 14, 2022 Revised manuscript received: December 1, 2022 Accepted manuscript online: December 7, 2022 Version of record online: January 9, 2023